

Contents lists available at ScienceDirect

# Journal of the Mechanical Behavior of Biomedical Materials

Journal of the Mechanical Behavior of Bornedical Materials

journal homepage: www.elsevier.com/locate/jmbbm

# A study on modeling the deflection of surgical needle during insertion into multilayer tissues

Samer Al-Safadi, Parsaoran Hutapea

Department of Mechanical Engineering, Temple University, Philadelphia, PA, USA

#### ARTICLE INFO

# Keywords: Needle insertion mechanics Needle insertion forces modeling Analytical needle deflection modeling Polyvinyl-chloride phantom tissues

#### ABSTRACT

The use of subcutaneous and percutaneous needle and catheter insertions is standard in modern clinical practice. However, a common issue with bevel tip surgical needles is their tendency to deflect, causing them to miss the intended target inside the tissue. This study aims to understand the interaction between the needle and soft tissue and develop a model to predict the deflection of a bevel tip needle during insertion into multi-layered soft tissues. The study examined the mechanics of needle-tissue interaction and modeled the forces involved during insertion. The force model includes cutting force, deformation force, and friction between the needle and tissue. There was an 8%–23% difference between the total analytical and experimental force measurements. A modified Euler-Bernoulli beam elastic foundation theory was used to create an analytical model to predict the needle tip deflection in soft tissue. To validate the results, the analytical deflection model was then compared to the deflection from needle insertion experiments on multi-layered phantom tissues, showing a 9%–21% error between the two. While there is a slight discrepancy between the analytical and experimental results, the study shows that the proposed model can accurately predict needle tip deflection during insertion.

# 1. Introduction

Percutaneous needle insertion is a widely used procedure in open surgery, particularly for biopsies of abdominal tumors, breast cancer, and prostate cancer (Ahrar et al., 2014). Despite its popularity, the insertion of a needle into a target can be challenging due to the design of the needle tip, which can be easily deflected and cause the needle to miss its target. This can result in repeated procedures, leading to adverse tissue damage and potential damage to sensitive tissues such as nerves (Ravali and Manivannan, 2017). Therefore, predicting the needle's steering behavior during insertion into soft tissues is crucial.

Many researchers have attempted to simulate needle deflection in soft tissue by developing models that consider the tissue's deformation during needle insertion. For example, DiMaio et al. (DiMaio and Salcudean, 2003) and Goksel et al. (2006) measured planar tissue deformations in an experimental system during rigid needle insertion, while Webster et al. (2006) created a nonholonomic model based on a kinematic bicycle model for steering bevel tip needles. Alterovitz et al. (2005) used a 2D linear elastic model to simulate prostate tissue during a brachytherapy procedure, while Yamaguchi et al. (2014) developed a dynamic analysis model for needle insertion into soft materials using

finite element analysis. Assaad et al. (2015) proposed a finite element analysis based on the Johnson-Cook damage model. Lehmann et al. (2013) used the Euler-Bernoulli beam theory to model needle deflection under static force distribution. Misra et al. (2010) used an energy-based model to consider the nonlinearity of needle-tissue interaction. Yan et al. (2008) showed the nonlinearity of the needle-tissue interaction by considering this factor. Dash et al. (2008) modeled the needle as a cantilever beam supported by a series of nonlinear springs and assumed the modified p-y curve method. According to a deflection model, Rossa et al. (2016) proposed an optimal path-planning method for flexible needle insertion to increase the needle targeting accuracy, and Huo et al. (2012) proposed a motion-planning method for flexible needle insertion in multilayer tissue with obstacles. Jushiddi et al. (2021) presented a multilayer tissue model using a coupled Eulerian-Lagrangian-based finite element method to simulate the motion of a flexible hollow bevel-angled needle into porcine liver tissue. Normally, the computational time for the analytical model is much less compared to models based on finite element methods.

Many previous studies aimed to assist percutaneous needle insertion using robotic systems to target the prostate, liver, and breast (Franco et al., 2015; Su et al., 2014; Bassan et al., 2009). In the case of needle

E-mail address: hutapea@temple.edu (P. Hutapea).

<sup>\*</sup> Corresponding author.

insertion into multilayer tissues, Computerized Tomography (CT) and Magnetic Resonance Imaging (MRI) are generally used as medical image guidance modalities for creating a preoperative insertion path plan and placing the needle tip in the correct anatomical position during insertion. Although both imaging modalities can deliver high-resolution and low-noise images, it is difficult to track the needle and target position in real-time with CTs and MRIs. Therefore, a surgeon typically uses a trial-and-error method with a step-and-shoot approach in clinical practice. An insertion, in this case, is divided into several steps with image scanning at each step (Hamzé et al., 2016); typically, this procedure shows low efficiency and low accuracy. Hence, it is helpful to predict the needle deflection and preoperatively plan the insertion trajectory. The preoperative method can be employed to acquire the mechanical characteristics and parameters of the needle-tissue system. These parameters can be analyticity or experimentally measured and used as inputs for modeling the deflection of the needle during the insertion into multilayer tissues. Consequently, there is no need for real-time feedback of estimated system states for updating the model parameters.

The presented research paper provides significant advancements in the understanding of needle steering in soft tissues, a crucial aspect of medical procedures such as biopsies and needle-based interventions. This work offers invaluable analytical techniques for calculating the forces between needle and tissue and predicting needle deflection. Preoperative data, including tissue-specific parameters and the geometric and material properties of the needle, is utilized in this research. This data-driven approach facilitates accurate modeling of needle deflection, standing in contrast to models that require real-time feedback. As a result, an efficient and resource-effective method is created, with computational software like MATLAB used for estimations. This method notably reduces computational time when compared to finite element method, which are known to demand extensive processing resources. An answer is given for a novel experimental setup that uses a multilayered tissue-mimicking method to simulate needle insertions. This approach bridges the gap between synthetic and real-world conditions, allowing for a nuanced understanding of needle-tissue interactions. The Euler-Bernoulli beam on elastic foundation theory (Al-Safadi and Hutapea, 2021) is adapted to consider the effects of needle-tissue interaction forces in a multilayer soft tissue environment. This approach effectively handles the nonlinear properties of tissues and captures the complex needle-tissue dynamics (James and Pai, 1999). Two essential concepts are underlined in the proposed model: firstly, the preoperatively obtained information is leveraged to account for the tissue's nonlinear properties via a multilayer tissue model. Secondly, the needle insertion process is treated as quasistatic, thereby ignoring needle insertion dynamics, viscoelastic tissue behavior, and the effects of insertion velocity on interaction forces (Mahvash and Dupont, 2009). This work achieves improved precision and understanding of needle-tissue interactions and the predicted deflections of needles in multilayer tissues. The potential implications of this research are promising improvements in procedure safety, accuracy, and patient outcomes.

#### 2. Materials and methods

In this section, the needle-tissue interaction cutting, friction, and tissue deformation forces were investigated and analytically calculated. Euler-Bernoulli beam theory (Al-Safadi and Hutapea, 2021; Khadem et al., 2015) was utilized to create an analytical model of needle deflection under needle-tissue interaction forces.

# 2.1. Needle-tissue interaction forces

The needle-tissue interaction forces during needle steering in soft tissue after the needle is fully inserted can be characterized into three groups (Jiang et al., 2014a). The cutting force  $F_c$  occurs after the crack propagates into the tissue in response to the needle tip displacement

(Okamura et al., 2004). The friction force  $F_f$  is the interaction force on the interface between the tissue and the needle surfaces. The tissue deformation force  $F_s$  which is a distributed force used to model tissue reaction forces resulting from its deformation caused by needle bending (Khadem et al., 2016). A schematic of a bevel-tip needle and its interaction with the soft tissue is shown in Fig. 1.

These three forces, the cutting force, the friction force, and the tissue deformation force, affect the needle deflection during insertion (Khadem et al., 2015), which were evaluated in this study. This study did not consider the puncture force, which happens when the needle pierces the tissue.

# 2.1.1. Cutting force

The tissue cutting starts after the needle tip is entirely inserted into the tissue (Khadem et al., 2016). During the tissue cutting, a force distribution resulting from the needle tip interaction with the soft tissue will show on the needle tip. For a solid bevel tip needle, this tissue cutting force, which has a triangle distribution due to the bevel shape, will be used to calculate the cutting force. After the needle tip is fully inserted, the crack length (a) will become the needle tip length. The crack tip opening displacement will be defined as  $(\delta)$  can be calculated as:

$$\delta = 2a \tan \frac{\alpha}{2} \tag{1}$$

Where  $\alpha$  is the needle tip angle Fig. 1. The cutting force (Fc) can be calculated in Equation (2):

$$F_{c} = \int_{0}^{a} E_{T} \delta da$$
 (2)

Where  $E_T$  is the tissue stiffness per unit length.

From Equations (1) and (2), the cutting force for an elastic tissue deformation can be expressed as Equation (3):

$$F_{c} = E_{T} \tan\left(\frac{\alpha}{2}\right) a^{2} \tag{3}$$

## 2.1.2. Friction force

The distributed force along the needle axis can be modeled as modified Winkler's foundation with foundation modulus (Yankelevsky et al., 1989) as shown in Equation (4):

$$F_{n} = k\Delta L \tag{4}$$

Where  $F_n$  is the distributed normal force along the needle shaft due to the tissue deformation,  $\Delta$  is the settling amount, k is the foundation modulus, and L is the length of the needle inside the tissue.

The foundation modulus of an elastic beam (Biot, 1937), (Jiang et al., 2014b) can be expressed as:

$$k = \frac{0.65E_2}{1 - \nu_2^2} \sqrt[12]{\frac{E_2(b)^4}{E_1I(1 - \nu_2^2)}}$$
 (5)

Where I and b are the moment of inertia of the needle and foundation width, respectively.  $E_1$ ,  $E_2$  and  $\nu_1$ ,  $\nu_2$  are the Young's modulus and the Poisson ratio of needle and soft tissue, respectively.

Using the Coulomb friction definition, the friction force acting on the needle shaft can be described as:

$$F_{f} = \mu F_{n} \tag{6}$$

Where  $\mu$  is the friction coefficient between the needle and the soft tissue. Substituting Equation (4) in Equation (6)

$$F_{f} = \mu k \Delta l = \mu \left[ \frac{0.65 E_{2}}{1 - \nu_{2}^{2}} \sqrt[12]{\frac{E_{2}(b)^{4}}{E_{1}I(1 - \nu_{2}^{2})}} \right] \Delta L$$
 (7)

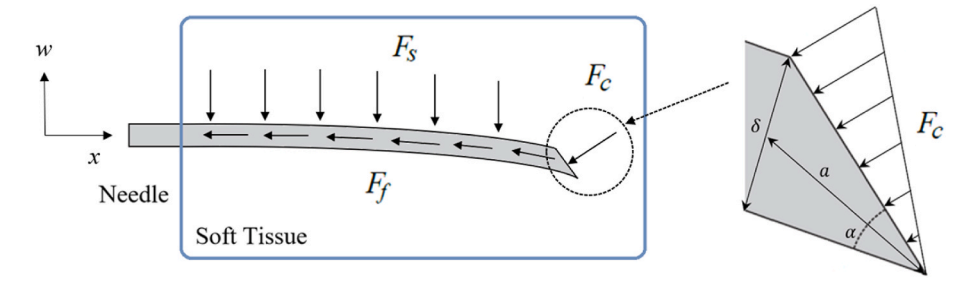


**Fig. 1.** Needle-tissue interaction forces during the insertion of bevel-tip needle into a soft tissue, (a) is the needle tip length,  $(\delta)$  is the crack tip opening displacement,  $(\alpha)$  is the needle tip angle.

Having the foundation width  $b=\pi d$  (i.e., the circumference of the needle circular cross-sectional area), and  $\Delta=\frac{d}{2}$  (where d is the diameter of the needle).

The model for the friction force can be written as Equation (8):

$$F_{\rm f} = \frac{\mu d}{2} \frac{0.65 E_2}{1 - \nu_2^2} \sqrt[12]{\frac{E_2(\pi d)^4}{E_1 I(1 - \nu_2^2)}} L \tag{8}$$

#### 2.1.3. Tissue deformation force

A force distribution profile can be used to model the needle-tissue interaction (Khadem et al., 2015). The tissue reaction forces applied to the needle are the same along the shaft of the needle and can be presented with a uniformly distributed force. The tissue-needle interaction force can be found as Equation (14):

$$F_s = kw (9)$$

Where k is the foundation modulus expressed in Equation (10), and w is the deflection of the needle in the vertical direction.

The cutting, friction, and tissue deformation forces defined previously were utilized to create an analytical needle deflection model using Euler-Bernoulli Beam theory, as shown in the next section.

#### 2.2. Needle deflection analytical model

The needle used in this study was a solid needle modeled as a Euler-Bernoulli beam translating along its longitudinal axis with the following assumptions: the deflection of the needle is small compared to its length, and its weight is neglected. The needle bending is planar, and in-plane axial bending and rotation of beam elements are negligible. The needle is a long thin cantilever beam with a constant cross-section clamped from one side and free on the other side. The beam length to thickness ratio is much greater than 10. The needle moves with a constant velocity.

Euler-Bernoulli beam theory was utilized with the previous assumptions to model the needle as a cantilever beam resting on an elastic

foundation and acquire a governing equation to estimate the needle deflection during the insertion. This beam undergoes various external loads resulting from the needle-tissue interaction explained in Section 2.2, where the cutting, friction, and tissue deformation forces were expressed in Equations (3), (8) and (9), respectively. Since the model is trying to predict the deflection of the needle in the vertical direction, only the transverse components of the forces we considered in the model, the cutting and friction were expressed as  $F_{c,y}$  and  $F_{f,y}$  as shown in Fig. 2.

Where  $\alpha$  is the needle tip angle,  $\theta$  is the needle rotation angle,  $\theta_L$  is the rotation angle at the end of the needle, and  $\gamma = \alpha + \theta_L$ . Using these parameters, the cutting and friction can be described in Equations (10) and (11) as:

$$F_{c,y} = F_c \cos \gamma \tag{10}$$

$$F_{f,y} = \int_0^L F_f \sin \theta dx \tag{11}$$

Where L is the length of the needle inside the tissue.

From the Euler-Bernoulli beam theory, the governing equation for the needle deflection in the vertical direction can be written as Equation (12):

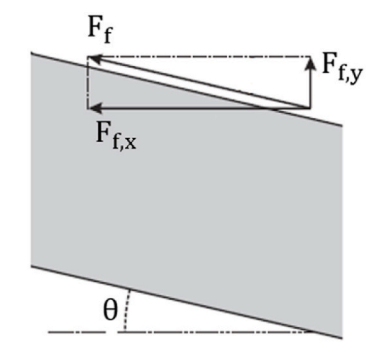
$$\frac{\partial^2}{\partial x^2} EI\left(\frac{\partial^2 w(x)}{\partial x^2}\right) + F_s = F_{f,y} + F_{c,y} \tag{12} \label{eq:12}$$

Where w is the deflection of the needle in the vertical direction.

To simplify Equation (12),  $F_{c,y}$ , and  $F_{f,y}$  were expressed as F. Substituting the tissue deformation force ( $F_s$ ) from Equation (9) in Equation (12), The governing equation for a needle deflection on an elastic foundation can be described as Equation (13):

$$\frac{\partial^{2}}{\partial x^{2}} EI\left(\frac{\partial^{2} w(x)}{\partial x^{2}}\right) + kw(x) = F$$
(13)

Dividing Equation (13) by EI and letting  $\beta^4 = \frac{k}{4EI}$ :



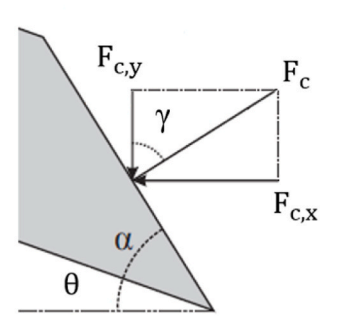


Fig. 2. The cutting and friction forces acting on the needle during the insertion.

$$\frac{\partial^4 \mathbf{w}}{\partial \mathbf{x}^4} + 4\beta^4 \mathbf{w} = \frac{\mathbf{F}}{\mathbf{FI}} \tag{14}$$

The complementary part of Equation (14) can be written as:

$$\frac{\partial^4 \mathbf{w}}{\partial \mathbf{x}^4} + 4\beta^4 \mathbf{w} = 0 \tag{15}$$

Solving Equation (15) by assuming  $w = Ae^{\lambda x}$  and  $e^{\beta x_i} = \cos(\beta x) + i\sin(\beta x)$ :.

$$w = \cos(\beta x) (C_1 e^{\beta x} + C_3 e^{-\beta x}) + \sin(\beta x) (C_2 e^{\beta x} + C_4 e^{-\beta x})$$
(16)

The solution for  $\lambda$  in can be expressed as:

$$\lambda_{k+1} = 2\beta \left[ \cos \frac{(\pi + 2k\pi)}{4} + i \sin \frac{(\pi + 2k\pi)}{4} \right]$$
 (17)

Finally, the solution for the governing Equation (18) can be written as:

The boundary conditions of a cantilever beam fixed from one end (Fig. 1) are:

$$w(0) = 0, \frac{\partial w}{\partial x}(0) = 0, \frac{\partial^2 w}{\partial x^2}(L) = 0, \frac{\partial^3 w}{\partial x^3}(L) = 0$$

$$(19)$$

The boundary conditions from Equation (24) were used to find the four unknown constants  $(D_1, D_2, D_3, D_4)$  in Equation (18):

$$D_1 = -\frac{F}{k}, D_2 = -D_3 \tag{20}$$

$$D_{3}=-\frac{F}{\textit{k}}\left(\frac{cos(\beta L)sin(\beta L)+sinh(\beta L)cosh(\beta L)}{2+cosh(\beta L)^{2}}\right) \tag{21}$$

$$D_4 = -\frac{q}{k} \left( \frac{\cos(\beta L)^2 - \cosh(\beta L)^2}{\cos(\beta L)^2 + \cosh(\beta L)^2} \right)$$
(22)

By substituting Equations 20–22 in Equation (18), the needle deflection can be calculated using a numeric computing software MATLAB (MathWorks, Natick, MA). Equation (18) can be utilized to calculate the needle deflection analytically for different tissue compositions by adjusting each layer elastic property and length in the deflection model. The needle-tissue interaction forces analytically defined in Section 2.2 can be acquired utilizing the tissue elastic modulus of each layer and their corresponding length. The friction force is related to the length of the layer, whereas the cutting force is calculated using the properties of the layer where the needle tip is located. For example, in the case of needle insertion in a two-multilayer tissue, shown in Fig. 3, the cutting force is calculated using the properties of the second layer, where the friction forces  $F_{\Gamma 1}$ ,  $F_{\Gamma 2}$  come from the first and second layers, respectively.

Similarly, a model of needle insertion in a four-multilayer tissue is shown in Fig. 3, the friction forces  $F_{f1}$ ,  $F_{f2}$ ,  $F_{f3}$ ,  $F_{f4}$  are dependent of distances  $x_1$ ,  $x_2$ ,  $x_3$ ,  $x_4$ , respectively.

# 2.3. Multilayer tissue-mimicking phantoms

The experiments were performed to validate the precision of the needle deflection model. This work used a tissue-mimicking method to make phantom blocks representing human tissues. These tissues were manufactured using PVC, a common tissue-mimicking material for needle insertion research. PVC Tissue-mimicking materials are widely used as clinical simulators because they mimic biological tissues structural characteristics and mechanical properties, are relatively low cost, easy to manufacture, and are convenient (Chatelin et al., 2020). Some limitations of using PVC phantom tissues are that the mechanical and imaging properties of the PVC phantom tissues will slowly change over time. Also, PVC phantom tissues do not have water within the structure, which often results in a higher friction coefficient than biological soft tissues (McGarry et al., 2020; Li et al., 2016).

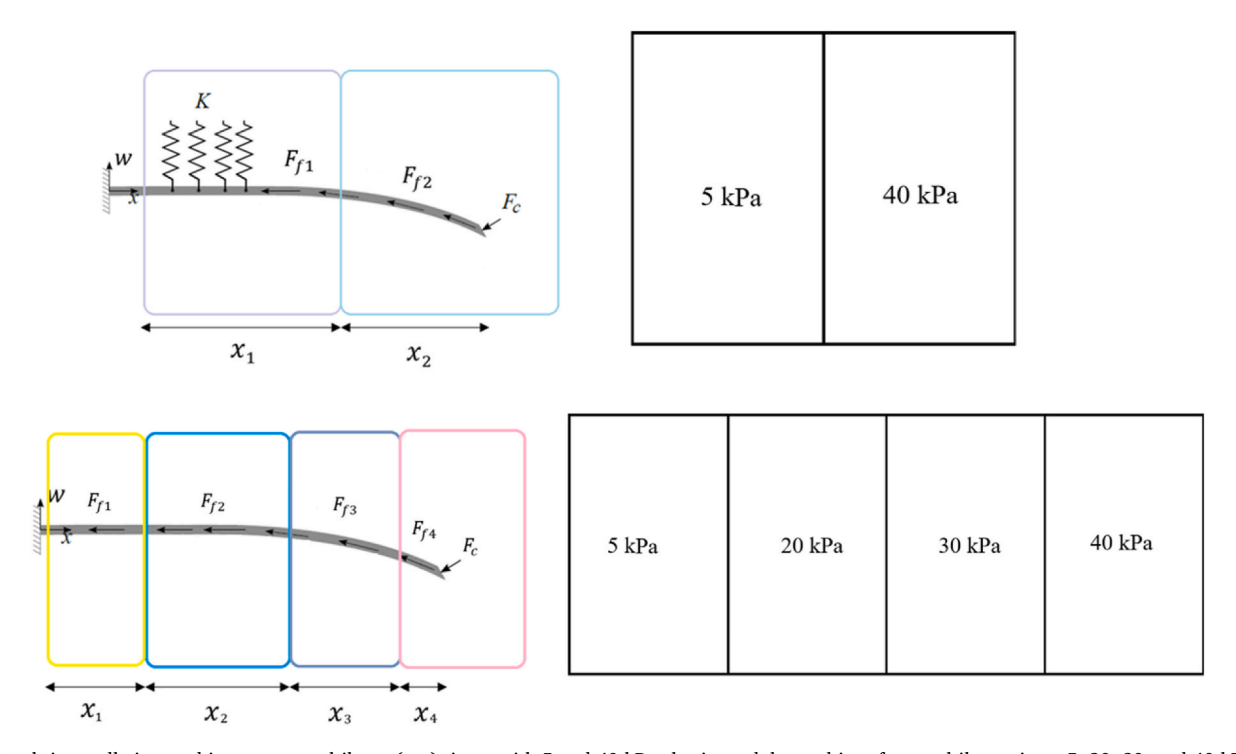


Fig. 3. Bevel-tip needle inserted into a two multilayer (top) tissue with 5 and 40 kPa elastic modulus and into four multilayer tissue 5, 20, 30, and 40 kPa elastic modulus (bottom).

The PVC polymer and a softener (both by M-F Manufacturing, Ft. Worth, Texas, USA) were blended to create the phantom materials. When the mixture is heated to 100 °C and stirred, it will polymerize and become transparent. Then, it is left to cool to room temperature for one day before transferring into a phantom block (Gidde et al., 2020). Several variations of PVC phantoms were needed to manufacture parts that have properties very similar to those of biological multilayer soft tissues. In (Van Houten et al., 2003; Öpik et al., 2012; Chen et al., 2016), phantom tissue materials were used to mimic biological tissues in the human body. These tissues include organs like the liver, kidney, fat, brain, muscles, and some parts of the skin, and their elastic modulus ranges from 5 kPa for the brain to 50 kPa for the kidney and the dermis. In this study, we selected a range of 5, 20, 30, and 40 to kPa that can represent a variety of human tissues. There are two sets of phantom tissues. The first multilayer phantom tissue setup consisted of two layers: the dermis with 40 kPa and the fat layer with 5 kPa. The second multilayer consisted of four layers: two layers of the dermis with a range of 30 and 40 kPa and two layers of fat with 5 and 20 kPa. That was achieved by adjusting the mass ratio between softener and PVC polymer solution (Li et al., 2015), the hardener-to-softener ratios used to make the phantom tissues were 90%/10%, 80%/20%,70%/30%, and 40%/60%.

Four PVC phantom blocks with different mechanical properties were prepared to make the multilayer phantom blocks. The layers were connected by slicing the phantom tissue blocks using cutting tools into smaller blocks with the required dimensions. The small blocks were connected by heating the sides of the blocks that formed the separation surface between the different layers using a heat gun. The heating temperature was high enough to get the PVC block surface to its melting point. Then they were compressed together to fabricate the multilayer phantom tissue block. Each layer had a width of 150 mm, a height of 55 mm, and a depth of 30 mm.

## 2.4. Experimental setup

The research performed in this paper involves conducting compression tests to verify the elastic modulus of the various phantom tissues, performing needle insertion experiments to quantify the interaction forces, and conducting additional needle insertion experiments to estimate the needle deflection. The tissue elastic modulus was tested for needle insertion in compression, not tension. Soft tissue primarily experiences compression and shear forces during needle insertion rather

than tension (Misra et al., 2010; Okamura et al., 2004). The elastic modulus quantifies the stiffness of a material by assessing its stress and strain relationship. During the insertion process, the tissue undergoes compression and cutting as the needle pushes and slides through it.

To determine the elastic modulus of each phantom tissue through compression tests, a Mini 55 (Instron Corporation, Norwood, MA) compression machine was employed. Three samples of PVC material were prepared, each with a height of 20 mm and a diameter of 40 mm. The compression machine's actuator drove the anvil to compress the sample at a speed of 0.2 mm/s, resulting in a compression of 4 mm. The elastic modulus of the PVC material was calculated by averaging the results obtained from these three samples.

As shown in Fig. 4, the needle deflection experimental setup consists of a linear actuator with a motor (Nema 23 CNC Stepper Motor) used to translate the needle along the insertion direction and a needle holder with the needle attached to it. A holder with a grid at the bottom and a polyvinyl chloride (PVC) gel phantom block inside it.

For the force measurement experimental setup, a 6 DOF F-T force sensor Nano17® (ATI Industrial Automation, Apex, NC) was attached to the base of the needle. The six-axis Nano17® transducer has a very-Fine resolution (down to 0.318 g-force) and is connected to a data acquisition system (National Instruments Corporation, Austin, TX). The force measurement experiments performed five horizontal sets of insertions and extraction into the phantom tissue with a velocity of 5 mm/s. The force sensor Nano17® records these insertion and extraction forces, and the force data is obtained using a programable data acquisition system utilizing LabVIEW (National Instruments Corporation, Austin, TX) software on a computer. The same computer controls the linear actuator displacement and velocity and performs the needle insertions and extractions in the phantom tissue. The same computer controls the linear actuator displacement and velocity and performs the needle insertions and extractions in the phantom tissue. Five sets of insertions and extraction were conducted horizontally with an insertion velocity of 5 mm/s and an insertion depth of 60 mm on four different phantom tissues with 5, 20, 30, and 40 kPa elastic modulus. The total time of each experiment was 16 s, where it initially took the needle 4 s to reach the surface of the tissue and 4 s after leaving the tissue to return to its original position. The needle-tissue interaction forces during the insertion and extraction were obtained using a data acquisition software program, LabVIEW, where the total number of samples used to measure the force during the whole crosses was 320 with a sample rate of 20.

This study utilized two multilayer tissue phantom setups to evaluate

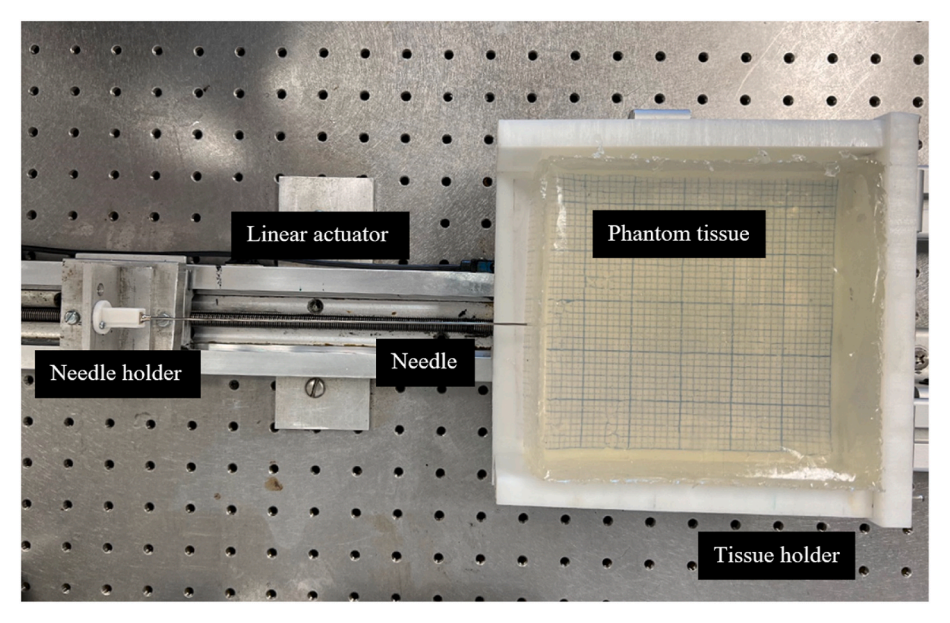


Fig. 4. Needle insertion experimental setup.

and observe needle deflection trends. These phantoms are composed of two PVC layers and four PVC layers. During the needle insertion experiment of the multilayer phantom tissues, the needle tip was first positioned to a starting point at the surface of the outer layer. Then, the needle penetrated the tissue with constant insertion speed and stopped when the needle tip reached the desired insertion distance. A camera located above the tested tissue is used to capture the actual needle deflection during the insertion. The needle insertion images, as shown in Fig. 5, were analyzed using the image processing software ImageJ (National Institute of Health, Bethesda, MD) to determine the deflection of the needle at its insertion point. For scaling the distances in ImageJ, a grid was placed under the tissues with a pixel length of 1/8 inch. The needle had a diameter of 1.62 mm, approximately equal to 0.0625 inches or 1/16 inch, and this value was selected as the precision for the deflection measurement, with an accuracy of  $\pm$  0.0625 inches. Accordingly, a pixel density of 16 pixels per inch (PPI) was required for the experiments. A camera, with its 12-megapixel resolution, was used to capture the deflection images with a resolution of  $3024 \times 4032$  pixels and an approximate pixel density of 800 PPI. The experiments involved using multiple needles with identical sizes and properties. The force measurements were performed five times for each phantom, and the deflection measurements were repeated three times. Two needles were assigned for the force experiments, while one needle was specifically designated for the deflection experiments. A solid needle was employed throughout the experiments, measuring 180 mm in length with a diameter of 1.62 mm. It featured a bevel-tip angle of 45° degrees and was constructed from stainless steel with a Young's Modulus of 200 GPa. Needle insertion velocity was set to 5 mm/s for all needle insertion experiments in PVC phantom tissues to minimize the effect of insertion velocity on the needle tissue interaction forces. Velocities higher than 5 mm/s will drastically increase the insertion force (Podder et al., 2006).

All PVC layers were transparent, allowing the needle tip to be visible for deflection measurement, as shown in Fig. 5, where the experimental deflection measurements were used to verify the results from the analytical deflection model. The total analytical force from cutting, friction, and tissue deformation was verified using force measurements obtained from needle insertion experiments. These measurements were conducted five times, and the average was calculated from the data points derived from these tests. The data from the force measurements, which was presented in its raw and unfiltered form, might be noisy. However, this approach was chosen to offer a realistic illustration of the forces encountered during needle-tissue insertion (Lehmann et al.,

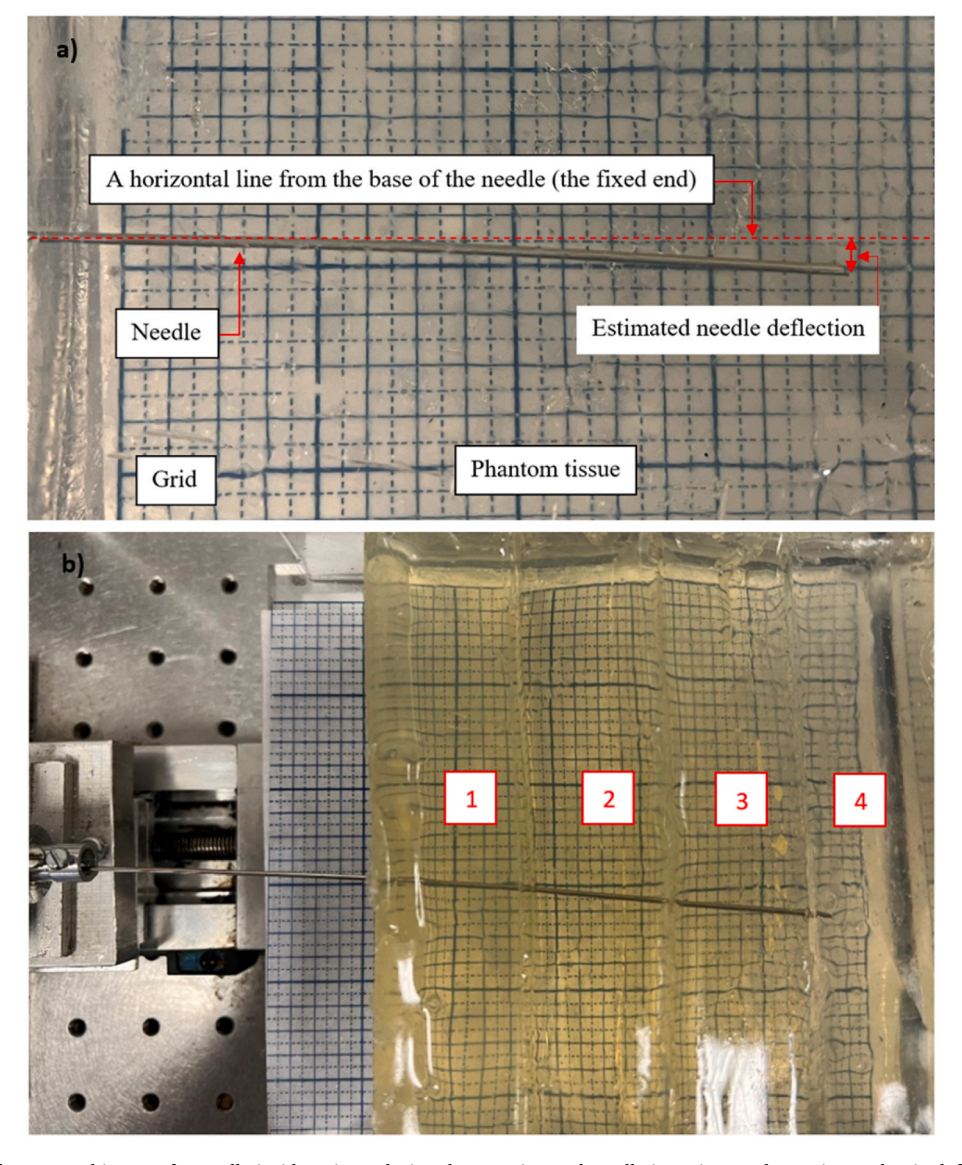


Fig. 5. A) An example of a captured image of a needle inside a tissue during the experimental needle insertion used to estimate the tip deflection. b) An example of experimental needle insertion into four multilayer tissues.

2013). The experimental force measurements from the needle extractions were used to confirm the analytical friction and tissue deformation forces. The previous study (James and Pai, 1999) developed an analytical predictive model for needle deflection in soft tissues. This model utilized the Euler-Bernoulli beam theory with an elastic foundation and a force model to predict the deflection of a needle into the tissue in single-layer tissues. The accuracy of the analytical model was confirmed by comparing the difference between the analytical model and the experimental results. The current research focuses on expanding this previous work (James and Pai, 1999), directed towards the prediction of needle deflection within multilayer tissue using the Euler-Bernoulli beam theory. The analytical deflection will be compared to experimental data to evaluate its accuracy.

#### 3. Results

#### 3.1. Measuring the needle-tissue interaction forces

The purpose of the force model was to predict the needle-tissue interaction forces during insertion through different layers of soft tissues. It was based on the three main force components discussed in Section 2: cutting, friction, and deformation. The force measurement setup, shown in Fig. 4, consisted of a linear actuator to perform the needle insertions and extractions in the tissue and a force sensor Nano17® attached to the base of the needle. To subtract any external forces generated by the weight of the needle and the vibrations of the needle, and its holder during the translational movement of the needle when it is being inserted into the tissue. Five insertion and extraction experiments were conducted on four different phantom tissues with elastic moduli of 5, 20, 30, and 40 kPa. Each test was performed with an insertion speed of 5 mm/s and a depth of 60 mm. From start to finish, every experiment took 16 s, including the 4 s it took for the needle to reach the tissue surface and the next 4 s for the needle to retract to its initial position post extraction. A necessary part of this experiment involved performing two distinct sets of needle insertions: one in the air and the other in the phantom tissue. The differential values obtained from these two scenarios served to further our understanding of the needle-tissue interaction forces, leading to a more refined calculation of these experimental forces. To acquire a more accurate description of the needle-tissue interaction forces, we took an average from these five sets of insertion and extraction tests. The data points plotted resulted from this averaging process, ensuring a more dependable representation of the forces involved.

The experimental force measurement results of the four phantom tissues are shown in Fig. 6. A curve of two parts presented the average insertion and extraction forces from the needle insertion in each phantom block. The top part indicates the insertion forces, and the bottom shows extraction forces. The insertion force starts from around 0 N, which presents the point where the needle penetrates the tissue up to maximum insertion force when the needle reaches the maximum insertion depth. Also, there is a maximum extraction point for the extraction phase, and it decreases to zero when the needle leaves the tissue. It is observed from the calculated experimental data that the extraction forces are 25–35% lower than the insertion forces due to the absence of the cutting force during the extraction stage.

The level of significance in the experimental force data was determined under the effect of the tissue elastic modulus. The maximum experimentally measured forces, in Fig. 6 Were statistically analyzed using one-way factorial ANOVA. The p-value was calculated for a significance level of  $\alpha=0.05.$  The hypothesis was used to determine if the mean values at the factor, the tissue elastic modulus, were statistically different. The p-value of 5.5E-19 was less than 0.05. The hypothesis was rejected, and the force measurements are statistically different and repeatable.

To verify the ability of the analytical force model to estimate the needle-tissue interaction forces, a curve representing the total analytical force consisting of cutting, friction, and tissue deformation was plotted along with an experimental insertion force. Since the analytical

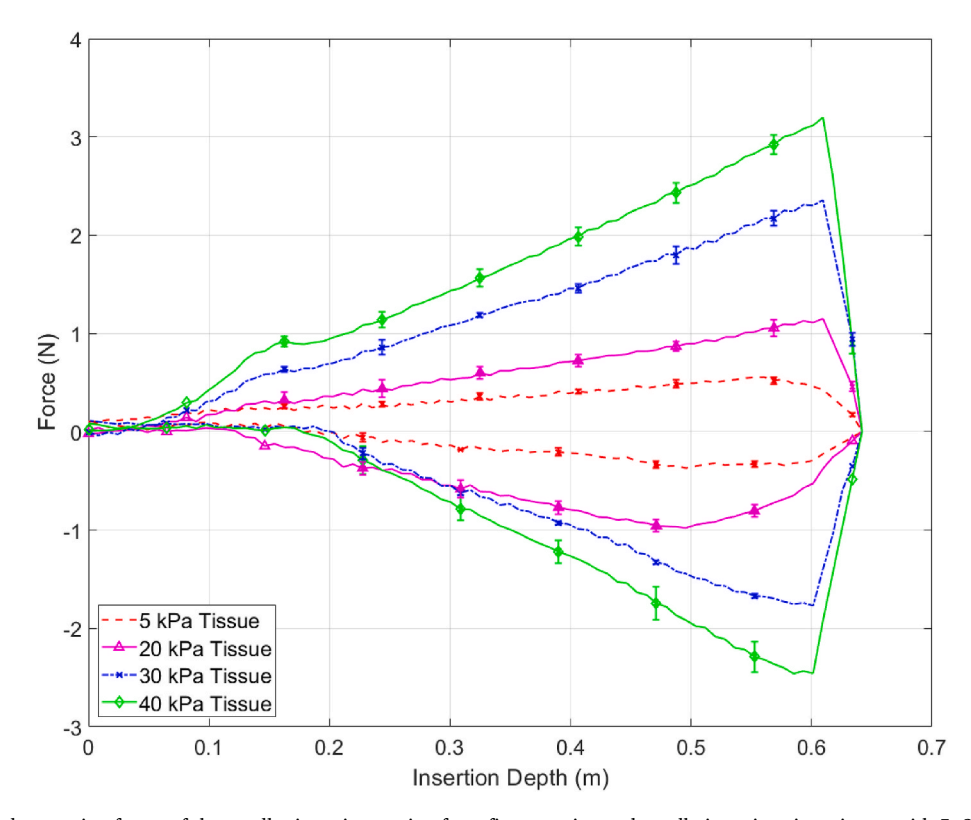
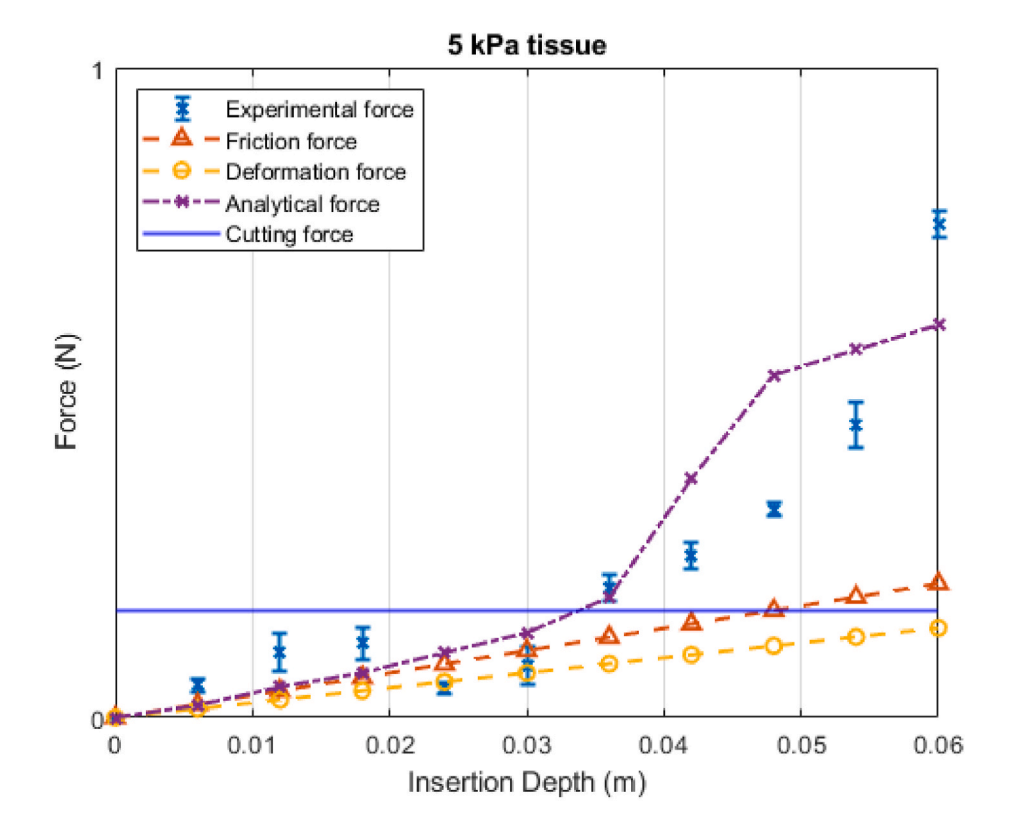


Fig. 6. The insertion and extraction forces of the needle-tissue interaction from five experimental needle insertions into tissues with 5, 20, 30, and 40 kPa elastic modulus with standard deviations ranges from 0.02 N to 0.1 N.

deflection model is based on predicting the deflection of the needle during the insertion, only the average insertion force, as shown in Figs. 7 and 8, was considered, and a separate analysis was constructed for four different phantom blocks with 5, 20, 30, and 40 kPa elastic modulus.

The analytical forces were based on the mechanical elastic property of the studied phantom block, and it was compared with its corresponding experimental total insertion force, as illustrated in Figs. 7 and 8.

In Figs. 7 and 8, the cutting, friction, and tissue deformation forces



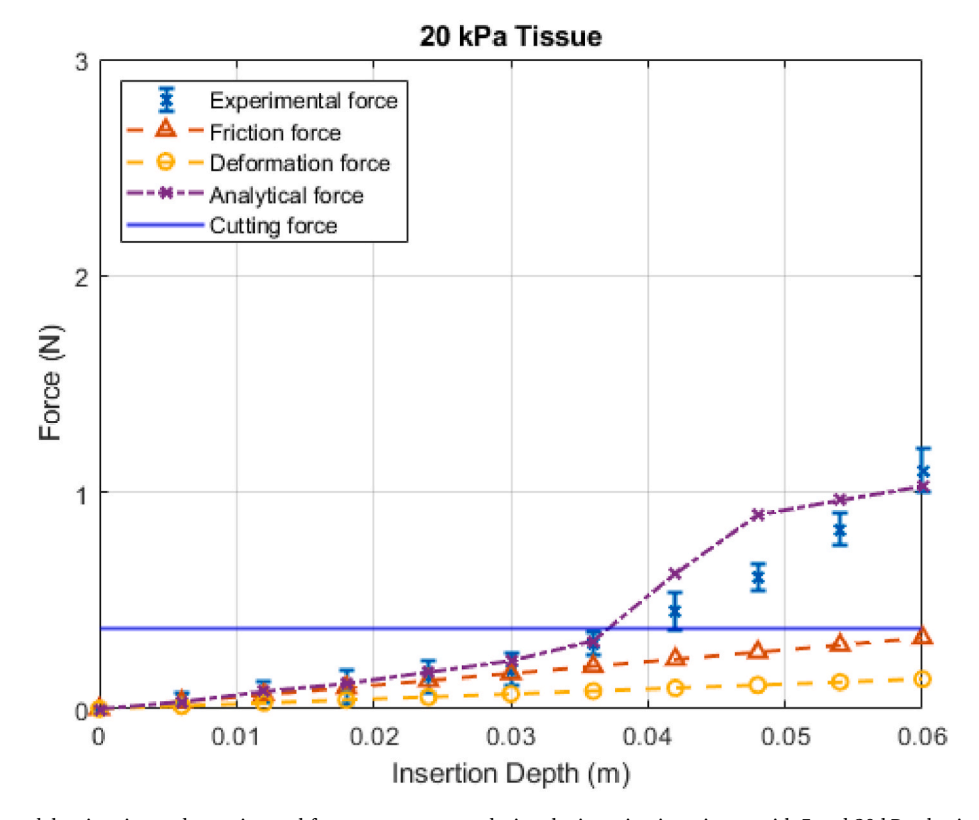
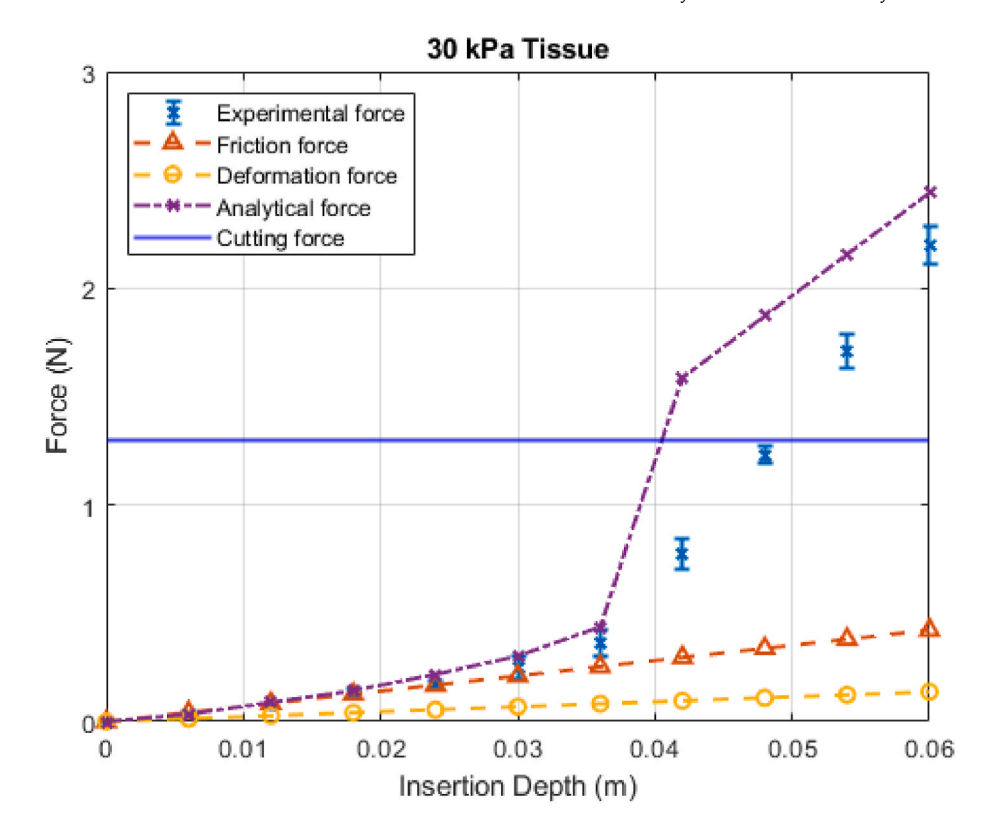


Fig. 7. Analytical force model estimation and experimental force measurements during the insertion into tissues with 5 and 20 kPa elastic modulus with a standard deviation range from 0.02 to 0.08 N.



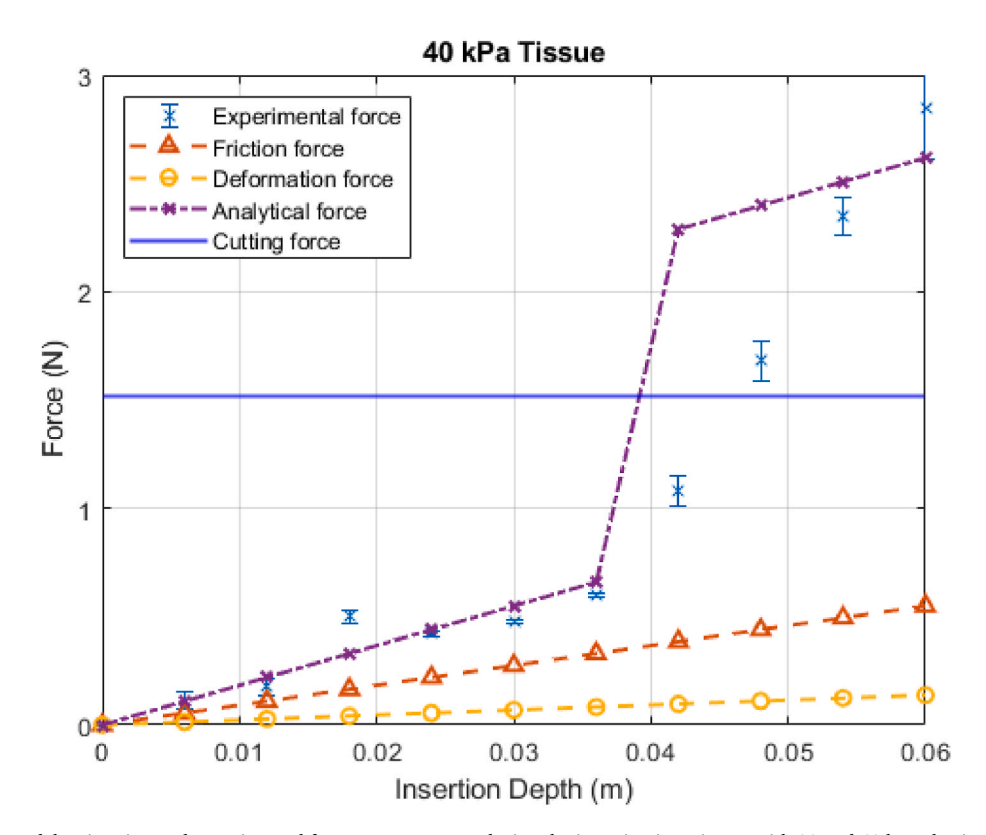


Fig. 8. Analytical force model estimation and experimental force measurements during the insertion into tissues with 30 and 40 kPa elastic modulus with a standard deviation range from 0.03 to 0.1 N.

were calculated separately using the analytical force models in Section 2. Since the needle insertion velocity was constant, the cutting force was constant and presented with a straight line, while the friction and tissue deformation forces increased with insertion depth. The total analytical

insertion force was created by combining the three previous forces and plotted next to the experimental insertion force. There is a nonlinear increase in the total force due to the needle puncture at the insertion entry point and then the rise of the cutting force, which occurs when the

**Table 1**Analytical and experimental force measurements difference.

Tissue elastic modulus	Insertion depth		
	30 mm	60 mm	
5 kPa	12%	11%	
20 kPa	23%	7%	
30 kPa	21%	11%	
40 kPa	16%	8%	

needle is completely inserted.

The difference in the total analytical force compared to the experimental force measurements was 8%–23%. Although this difference can lead to inaccurate analytical needle deflection calculations, the analytical force model values were used. The experimental results only show the total force. They cannot be used to find the magnitude of the cutting, friction, and tissue deformation forces needed in the analytical deflection solver. Therefore, the four phantom blocks analytical force estimations were used as inputs for the analytical needle deflection model during the insertion into multilayer phantom tissue. The comparisons between analytical and experimental force measurements are shown in Table 1.

#### 3.2. Measuring the analytical and the experimental needle deflections

To further understand needle-tissue interactions, experiments were conducted to study how needles behave when inserted into different tissue types. The focus was on the behavior of needles when inserted into tissues with varying elastic modulus levels. To ensure the accuracy of the results, three insertion tests at an insertion velocity of 5 mm/s and depth of 100 mm were performed for each level, with elastic modulus values of 5, 20, 30, and 40 kPa. The extent and direction of needle deflection were carefully noted during each test at regular intervals. The experimental needle deflection was estimated using ImageJ. After collecting the data was analyzed and revealed a clear relationship between tissue elastic

modulus and needle deflection. Fig. 9 shows the relationship between the insertion depth and the needle deflection for different tissue elastic moduli. As the elastic modulus increases (from 5 kPa to 40 kPa), the needle deflection increases for the same insertion depth. This suggests that the elastic modulus of the tissue significantly affects needle deflection as a higher elastic modulus offers greater resistance, leading to more deflection as the needle penetrates. An Analysis of Variance (ANOVA) test was performed to determine whether there were any statistically significant differences between the means of three or more independent groups. The ANOVA test yields an F-value of approximately 2.58 and a p-value of approximately 0.067. The p-value is more significant than the conventional significance level of 0.05. This suggests the null hypothesis cannot be rejected and that there is no significant difference in needle deflection between the tissue types at the 5% significance level, which declares a clear relationship between tissue elastic modulus and needle deflection.

In order to evaluate the performance of the proposed deflection model. That was performed by conducting needle insertion experiments in phantom tissue to stray the steering behavior of the needle, predict the needle deflection using the analytical model, and then compare the two sets of data to verify the model accuracy. There were two multilayer phantom tissue blocks compositions. The first consisted of parts with 5 kPa and 40 kPa elastic modulus. The second one was a four-layer tissue consisting of 5, 20, 30, 40 kPa. The reasoning behind the two different compositions was to study the effect of the number of layers on estimating the total deflection. During the needle insertion in the phantom tissue, the needle tip will cut through the tissue, allowing the needle to advance until it reaches the target. That process will leave a hollow path after the extraction of the needle. Fixing the entry point of the insertion will cause the needle to progress through this hollowed path, reducing the interaction between the needle and the phantom when the insertion is repeated. This will lead to smaller needle-tissue force values and affect the needle defecation estimation. The number of insertion tests conducted for all deflection experiments was three. The insertion distance for the two-layer tissue was 50 mm, and for the four-layer tissue, it was

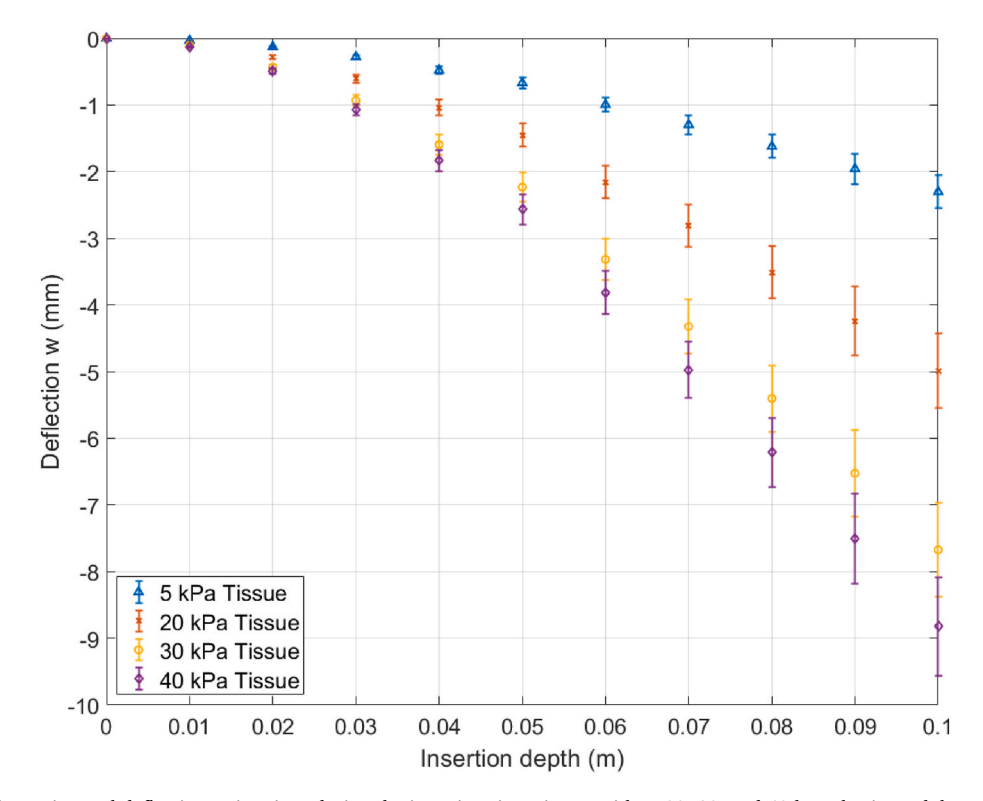


Fig. 9. Comparisons of experimental deflection estimations during the insertions into tissues with 5, 20, 30, and 40 kPa elastic modulus with a standard deviation range from 0.01 to 0.74 mm.

100 mm. All experiments had a constant insertion velocity of 5 mm/s. The average values of the needle deflection in the two-layer tissue are shown in Fig. 10, and for a needle deflection in the four-layers tissue in Fig. 11. These values were calculated using the model based on Euler-Bernoulli beam theory explained in the methods section with a force profile that presents the properties of 5 and 40 kPa layers which is demonstrated previously in the analytical force model. This model boundary conditions assumed that the insertion starts from the air and

the needle tip is in contact with the first layer surface where the entry point is. After the needle penetrates the tissue and travels through the phantom block, the entry point will become the fixed end of the needle, with the tip of the needle being the free end of the Euler-Bernoulli beam. Having preoperative measurements of the depth and properties of the layers and with the needle geometry and material property, the deflection of the needle can be computed at any point. For example, at an insertion depth of 40 mm (region 2 in Fig. 11), the length of the needle

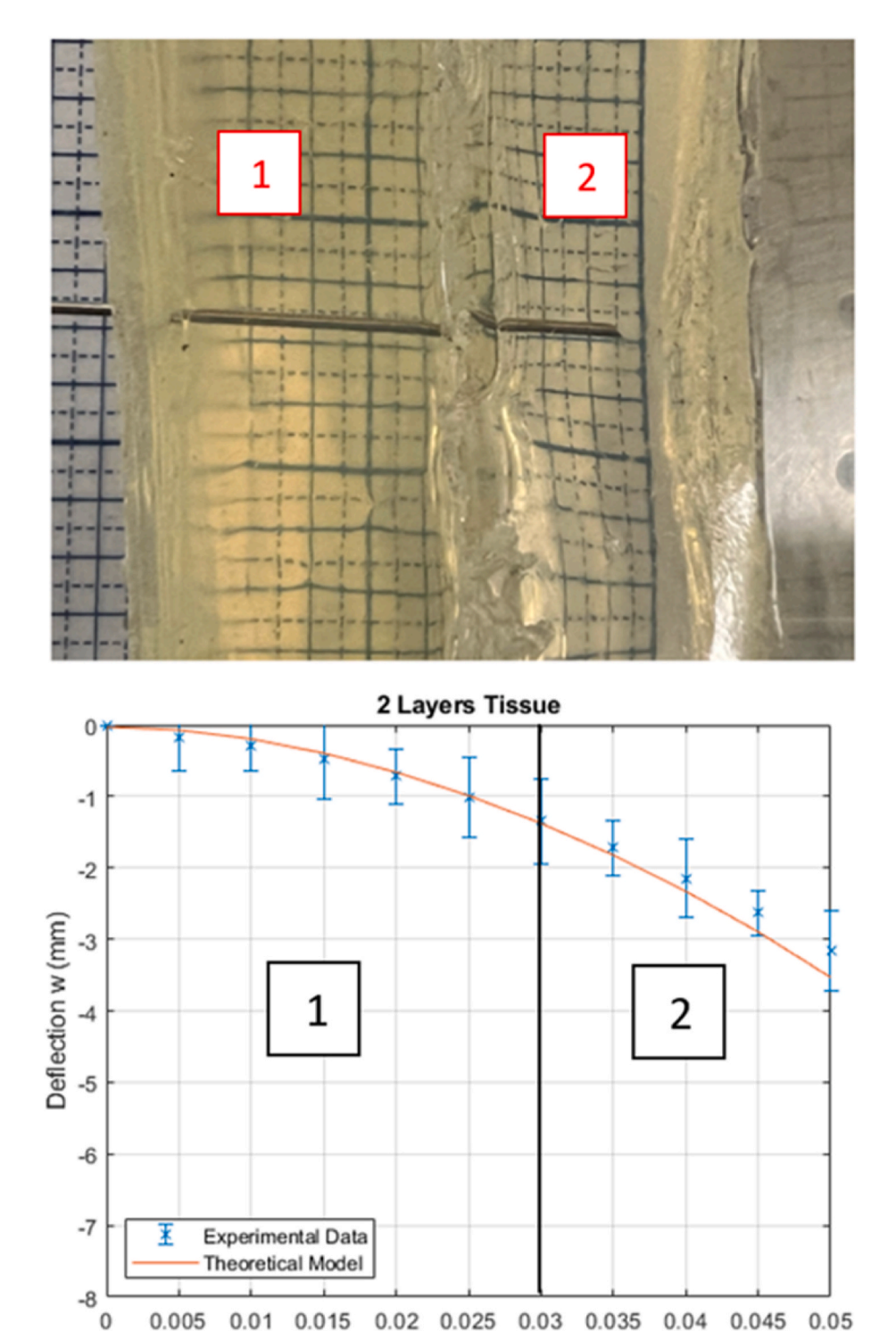


Fig. 10. Comparisons between the analytical deflection model predictions and experimental deflection estimations during the insertion into two-layers phantom tissue with a standard deviation of 0.42 mm.

Insertion depth (m)

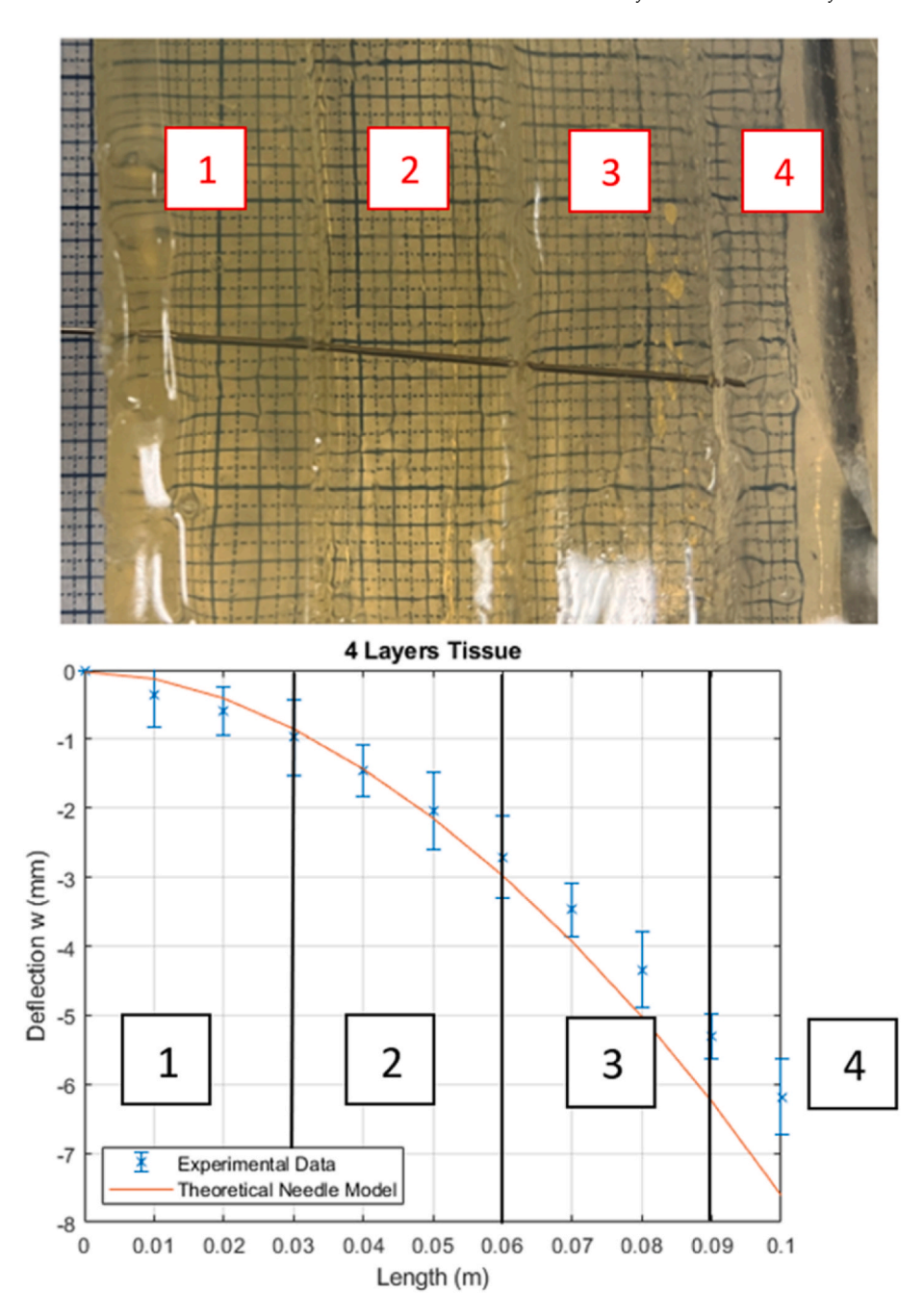


Fig. 11. Comparisons between the analytical deflection model predictions and experimental deflection estimations during the insertion into the four-layers phantom tissue with a standard deviation of 0.47 mm.

will be 40 mm, and the forces applied on the needle are the interaction results with 30 mm with a 40 kPa layer and 10 mm with a 5 kPa layer. The experimental needle deflection was estimated using ImageJ. The vertical dark line indicates the separation surface between the different layers. The analytical and the experimental deflections of the needle were plotted using MATLAB. Finally, this plot was utilized to compare the analytical deflection and experimental data.

#### 4. Discussion

Our results provide detailed insight into the dynamics of needletissue interaction during the insertion into soft tissues. As shown in Fig. 6, the forces required for extraction were 25–35% lower than those required for insertion due to the absence of the cutting force during extraction. This difference between insertion and extraction forces checks with the research performed by Patel et al. (2021), in which they observed a lower average maximum extraction force relative to the average maximum insertion force for an equal insertion depth.

The needle-tissue cutting force was simplified in this Study. The importance of this force during needle insertion was highlighted by Okamura et al. (2004) as they represented different approaches to understanding and predicting needle deflection during insertion into soft tissues. While our study simplifies the needle-tissue interaction, the cutting force model relied on simplified assumptions of elastic deformation, which may not fully capture the complex interactions between the needle and tissue. The cutting force estimation was achieved by utilizing a static mathematical model, producing a constant value in alignment with the research conducted by Khadem et al. (2016). Their study also featured a constant cutting force. However, it was determined using a more dynamic model. This model predicted a cutting force that

initially reduces with increased insertion depth and converges to a constant value.

The 8%-23% discrepancy, in Figs. 7 and 8, between the total analytical force and the experimental force measurements can be traced back to the simplicity of our cutting force modeling, which relied solely on elastic deformation assumptions. Including more accurate cutting force models could improve the accuracy of our analytical force predictions. In our analytical force calculations, this discrepancy is also derived from the cumulative effect of combining various forces, cutting, friction, and deformation. Each force component had its error and combining them amplified the differences between the model and the experiments. Enhancing the individual force models and reducing their respective errors could improve the accuracy of the total force estimation. Despite these discrepancies, it's important to note the model's accuracy for the study's purpose, given that the experimental results could not provide the individual force components necessary for a more accurate analytical deflection solution. Regarding experimental validation, the use of phantom tissues in this work aligns with other studies, such as that by Li et al. (2015), chosen due to their properties and ease of use. However, it is recognized that the mechanical properties of phantom tissues can significantly differ from actual biological tissues. Validation of the model could be more potent if experiments were extended to include biological tissues.

Additionally, an analysis of needle deflection was carried out in the study, where the Euler-Bernoulli beam theory was utilized to predict its behavior. This analytical model developed in our study for predicting needle deflection shares similarities with existing literature models while introducing unique factors that differentiate it. The Euler-Bernoulli beam theory is utilized in this model, as has been done in many studies, such as that by Khadem et al. (2015), to capture the needle's deflection during insertion. This theory provides a strong foundation for the model, enabling accurate capturing of the needle's fundamental mechanical behavior. However, alternative approaches, such as the Timoshenko or nonlinear beam theory, utilized in other work by Yan et al. (2008), might provide more precise predictions under specific conditions. In the work of Yan et al. they proposed a needle steering model that introduced depth-varying mean parameters to account for tissue inhomogeneity and used an online parameter estimator with a modified least square method and a forgetting factor, where our study presents a simplified model for predicting needle deflection based on analytical force models and the Euler-Bernoulli beam theory.

Another difference between our model and other models is observed in how the needle-tissue interaction is considered, such as the non-holonomic model proposed by Webster et al. (2006). The study of Webster et al. presented a 6-DOF nonholonomic model that predicts the path of a needle through phantom tissue based on the steering effect due to the asymmetry of the bevel tip and needs control systems with image feedback, even with the presence of a model, to cater to unmodelled tissue deformation and inhomogeneity. Our model simplifies the needle-tissue interaction and does not explicitly consider the asymmetry of the bevel tip, unlike the model by Webster et al. This could make our model easier to implement and interpret, but it may not capture certain specific phenomena related to the bevel tip.

The analytical predictions were compared with experimental data. In Figs. 9 and 10, the deflection was more definite after the needle passed through the separation surface between the two different elastic modulus layers in the two-layer tissue compared to the four-layer tissue. The comparison between analytical and experimental deflections revealed that the analytical model performed well in estimating the deflection in the first layer of the multilayer tissue block. However, as shown in Table 2, mismatches were observed in the third and the fourth layers in the four layers tissue.

Some other factors could affect the accuracy of the needle deflection prediction. For instance, the model assumes a constant insertion angle, while the actual insertion angle may change due to needle deflection in the previous tissue layer. Also, the deflection behavior might differ

 Table 2

 Analytical and experimental deflections comparisons.

Tissue composition	Analytical and experimental deflection difference				
	Region 1	Region 2	Region 3	Region 4	
Two-layers tissue	9%	12%	-	-	
Four-layers tissue	10%	12%	17%	21%	

depending on the stiffness of the tissue's last layer, which was not considered in our mode. Integrating these factors and investigating their impact on needle deflection estimation would enhance the accuracy of our model.

#### 5. Conclusion

An analytical force model to predict the needle-tissue interaction forces was presented in this work. The experimental setup measured the needle-tissue interaction forces, from cutting to friction and deformation. It was found that forces during extraction were 25–35% lower than during insertion, a finding attributable to the absence of the cutting force in the extraction phase. Our ANOVA analysis demonstrated that the force measurements were statistically different and repeatable, proving the experiment's reliability. A comparison of the experimental results with estimates from the analytical force model was subsequently made, and a discrepancy of 8%–23% was observed. Despite this discrepancy, the analytical force model values provided crucial insights into the individual cutting, friction, and tissue deformation forces involved in the needle deflection calculations.

Additionally, a model for predicting needle tip deflection within the tissue was introduced. The deflection model was based on the Euler-Bernoulli beam elastic foundation theory. Parameters such as the needle's geometry, material properties of the needle and tissue, and the distance to the tissue boundary, which can be determined from preoperative MRI images, were incorporated into the model. This study explored the deflection of needles upon insertion into different tissues. The elastic modulus of the tissue was found to significantly affect needle deflection, with a higher modulus resulting in increased deflection. This relationship offers a greater understanding of needle behavior during insertion into tissues of varying elastic modulus. The performance of the proposed deflection model was evaluated by conducting needle insertion experiments in multilayer phantom tissues. The comparison between the analytical and experimental results showed a difference of around 9%—21%.

Future enhancements to the model were identified, including considering viscoelastic mechanical properties and parameters such as insertion velocity, strain, and strain rate. More accurate modeling of boundary conditions and the separation surface could lead to more accurate predictions of needle-tissue interaction forces and needle deflection. While tissue-mimicking materials were used for measuring needle-tissue interaction forces and needle deflection, it was stated that future work would involve insertion tests into actual biological tissues. These tests are expected to better evaluate the proposed analytical deflection and force model results compared to experimental data.

## Credit author statement

Samer Al-Safadi: Writing – original draft. Parsaoran Hutapea: Writing – review & editing

#### **Declaration of competing interest**

The authors declare that they have no known competing financial interests or personal relationships that could have appeared to influence

the work reported in this paper.

#### Data availability

Data will be made available on request.

#### Acknowledgments

The authors would like to acknowledge the National Science Foundation (Civil, Mechanical and Manufacturing Innovation (CMMI) Award #1917711) for their financial support.

#### References

- Ahrar, J.U., Javadi, S., Ahrar, K., 2014. Percutaneous and transjugular kidney biopsy. In: Percutaneous Image-Guided Biopsy. Springer, New York, NY, pp. 257–266.
- Al-Safadi, S., Hutapea, P., 2021. An analytical model for predicting the deflection of hollow surgical needle in soft tissue. In: ASME International Mechanical Engineering Congress and Exposition, vol. 85598. American Society of Mechanical Engineers, V005T05A037.
- Alterovitz, R., Lim, A., Goldberg, K., Chirikjian, G.S., Okamura, A.M., 2005. Steering flexible needles under Markov motion uncertainty. In: 2005 IEEE/RSJ International Conference on Intelligent Robots and Systems. IEEE, pp. 1570–1575.
- Assaad, W., Jahya, A., Moreira, P., Misra, S., 2015. Finite-element modeling of a beveltipped needle interacting with gel. J. Mech. Med. Biol. 15 (5), 1550079.
- Bassan, H.S., Patel, R.V., Moallem, M., 2009. A novel manipulator for percutaneous needle insertion: design and experimentation. IEEE/ASME transactions on mechatronics 14 (6), 746–761.
- Biot, M.A., 1937. Bending of an Infinite Beam on an Elastic Foundation.
- Chatelin, S., Breton, E., Arulrajah, A., Giraudeau, C., Wach, B., Meylheuc, L., Vappou, J., 2020. Investigation of polyvinyl chloride plastisol tissue-mimicking phantoms for mr-and ultrasound-elastography. Frontiers in Physics 8, 522.
- Chen, A.I., Balter, M.L., Chen, M.I., Gross, D., Alam, S.K., Maguire, T.J., Yarmush, M.L., 2016. Multilayered tissue mimicking skin and vessel phantoms with tunable mechanical, optical, and acoustic properties. Med. Phys. (Woodbury) 43 (6Part1), 3117–3131.
- Dash, S.R., Bhattacharya, S., Blakeborough, A., Hyodo, M., 2008. PY curve to model lateral response of pile foundations in liquefied soils. In: 14th World Conference on Earthquake Engineering Beijing, pp. 12–17. China.
- DiMaio, S.P., Salcudean, S.E., 2003. Needle insertion modeling and simulation. IEEE Trans. Robot. Autom. 19 (5), 864–875.
- Franco, E., Brujic, D., Rea, M., Gedroyc, W.M., Ristic, M., 2015. Needle-guiding robot for laser ablation of liver tumors under MRI guidance. IEEE ASME Trans. Mechatron. 21 (2), 931–944.
- Gidde, S.T.R., Ciuciu, A., Devaravar, N., Doracio, R., Kianzad, K., Hutapea, P., 2020. Effect of vibration on insertion force and deflection of bioinspired needle in tissues. Bioinspiration Biomimetics 15 (5), 054001.
- Goksel, O., Salcudean, S.E., DiMaio, S.P., 2006. 3D simulation of needle-tissue interaction with application to prostate brachytherapy. Comput. Aided Surg. 11 (6), 270, 288
- Hamzé, N., Peterlík, I., Cotin, S., Essert, C., 2016. Preoperative trajectory planning for percutaneous procedures in deformable environments. Comput. Med. Imag. Graph. 47, 16–28.
- Huo, B., Zhao, X., Han, J., Xu, W., 2012. Motion planning for flexible needle in multilayer tissue environment with obstacles. In: 2012 IEEE International Conference on Systems, Man, and Cybernetics (SMC). IEEE, pp. 3292–3297.
- James, D.L., Pai, D.K., 1999. Artedi: accurate real time deformable objects. In: Proceedings of the 26th Annual Conference on Computer Graphics and Interactive Techniques, pp. 65–72.
- Jiang, S., Wang, X., Su, Z., 2014a. Mechanics-based bevel-tip needle deflection model during needle-soft tissue interaction process. J. Mech. Med. Biol. 14 (5), 1450076.

- Jiang, S., Li, P., Yu, Y., Liu, J., Yang, Z., 2014b. Experimental study of needle-tissue interaction forces: effect of needle geometries, insertion methods and tissue characteristics. J. Biomech. 47 (13), 3344–3353.
- Jushiddi, M.G., Mani, A., Silien, C., Tofail, S.A., Tiernan, P., Mulvihill, J.J., 2021.
  A computational multilayer model to simulate hollow needle insertion into biological porcine liver tissue. Acta Biomater. 136, 389–401.
- Khadem, M., Fallahi, B., Rossa, C., Sloboda, R.S., Usmani, N., Tavakoli, M., 2015.
  A mechanics-based model for simulation and control of flexible needle insertion in soft tissue. In: 2015 IEEE International Conference on Robotics and Automation (ICRA). IEEE, pp. 2264–2269.
- Khadem, M., Rossa, C., Sloboda, R.S., Usmani, N., Tavakoli, M., 2016. Mechanics of tissue cutting during needle insertion in biological tissue. IEEE Rob. Autom. Lett. 1 (2), 800–807.
- Lehmann, T., Tavakoli, M., Usmani, N., Sloboda, R., 2013. Force-sensor-based estimation of needle tip deflection in brachytherapy. J. Sens. 2013, 1–10. Article ID 263153
- Li, W., Belmont, B., Shih, A., 2015. Design and manufacture of polyvinyl chloride (PVC) tissue mimicking material for needle insertion. Procedia Manuf. 1, 866–878.
- Li, W., Belmont, B., Greve, J.M., Manders, A.B., Downey, B.C., Zhang, X., et al., 2016. Polyvinyl chloride as a multimodal tissue-mimicking material with tuned mechanical and medical imaging properties. Med. Phys. 43 (10), 5577–5592.
- Mahvash, M., Dupont, P.E., 2009. Mechanics of dynamic needle insertion into a biological material. IEEE (Inst. Electr. Electron. Eng.) Trans. Biomed. Eng. 57 (4), 934–943.
- McGarry, C.K., Grattan, L.J., Ivory, A.M., Leek, F., Liney, G.P., Liu, Y., et al., 2020. Tissue mimicking materials for imaging and therapy phantoms: a review. Phys. Med. Biol. 65 (23), 23TR01.
- Misra, S., Reed, K.B., Schafer, B.W., Ramesh, K.T., Okamura, A.M., 2010. Mechanics of flexible needles robotically steered through soft tissue. Int. J. Robot Res. 29 (13), 1640–1660
- Okamura, A.M., Simone, C., O'leary, M.D., 2004. Force modeling for needle insertion into soft tissue. IEEE Trans. Biomed. Eng. 51 (10), 1707–1716.
- Öpik, R., Hunt, A., Ristolainen, A., Aubin, P.M., Kruusmaa, M., 2012. Development of high fidelity liver and kidney phantom organs for use with robotic surgical systems. In: 2012 4th IEEE RAS & EMBS International Conference on Biomedical Robotics and Biomechatronics (Biorad). IEEE, pp. 425–430.
- Patel, K.I., Zhu, L., Ren, F., Hutapea, P., 2021. Effect of composite coating on insertion mechanics of needle structure in soft materials. Med. Eng. Phys. 95, 104–110.
- Podder, T.K., Clark, D.P., Fuller, D., Sherman, J., Ng, W.S., Liao, L., Rubens, D.J., Strang, J.G., Messing, E.M., Zhang, Y.D., Yu, Y., 2006. Effects of velocity modulation during surgical needle insertion. In: 2005 IEEE Engineering in Medicine and Biology 22th Annual Conference, IEEE, pp. 5766–5770.
- 27th Annual Conference. IEEE, pp. 5766–5770.

  Ravali, G., Manivannan, M., 2017. Haptic feedback in needle insertion modeling and simulation. IEEE reviews in biomedical engineering 10, 63–77.
- Rossa, C., Usmani, N., Sloboda, R., Tavakoli, M., 2016. A hand-held assistant for semiautomated percutaneous needle steering. IEEE (Inst. Electr. Electron. Eng.) Trans. Biomed. Eng. 64 (3), 637–648.
- Su, H., Shang, W., Cole, G., Li, G., Harrington, K., Camilo, A., et al., 2014. Piezoelectrically actuated robotic system for MRI-guided prostate percutaneous therapy. IEEE/ASME transactions on mechatronics 20 (4), 1920–1932.
- Van Houten, E.E., Doyley, M.M., Kennedy, F.E., Weaver, J.B., Paulsen, K.D., 2003. Initial in vivo experience with steady-state subzone-based MR elastography of the human breast. J. Magn. Reson. Imag.: An Official Journal of the International Society for Magnetic Resonance in Medicine 17 (1), 72–85
- Magnetic Resonance in Medicine 17 (1), 72–85.

  Webster III, R.J., Kim, J.S., Cowan, N.J., Chirikjian, G.S., Okamura, A.M., 2006.

  Nonholonomic modeling of needle steering. Int. J. Robot Res. 25 (5–6), 509–525.
- Yamaguchi, S., Tsutsui, K., Satake, K., Morikawa, S., Shirai, Y., Tanaka, H.T., 2014. Dynamic analysis of a needle insertion for soft materials: arbitrary Lagrangian–Eulerian-based three-dimensional finite element analysis. Comput. Biol. Med. 53, 42–47.
- Yan, K.G., Podder, T., Yu, Y., Liu, T.I., Cheng, C.W., Ng, W.S., 2008. Flexible needle–tissue interaction modeling with depth-varying mean parameter: preliminary study. IEEE (Inst. Electr. Electron. Eng.) Trans. Biomed. Eng. 56 (2), 255–262.
- Yankelevsky, D.Z., Eisenberger, M., Adin, M.A., 1989. Analysis of beams on nonlinear winkler foundation. Comput. Struct. 31 (2), 287–292.